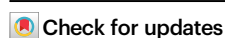


# Unconventional (anti)ferroelectricity in van der Waals group-IV monochalcogenides

Received: 8 September 2024

Accepted: 13 February 2025

Published online: 20 February 2025



Fengrui Sui<sup>1,3</sup>, Yilun Yu<sup>1,3</sup>, Ju Chen<sup>2,3</sup>, Ruijuan Qi<sup>1</sup>✉, Rui Ge<sup>1</sup>,  
Yufan Zheng<sup>1</sup>, Beituo Liu<sup>1</sup>, Rong Jin<sup>1</sup>, Shijing Gong<sup>2</sup>✉, Fangyu Yue<sup>1</sup>✉ &  
Junhao Chu<sup>1</sup>

Fundamentally, ferroelectrics must belong to a noncentrosymmetric space group, limiting the exploration of more new ferroelectric materials. We circumvent this limitation by triggering structure distortion and inducing ferroelectricity in centrosymmetric van der Waals group-IV monochalcogenide GeSe semiconductor that features unexpected intrinsic out-of-plane antiferroelectricity. Double-type and single-type hysteresis loops from electric measurements, bonding distortion observed in in-situ atomic imaging, and perpendicular polarization uncovered by first-principles calculations, confirm the intrinsic out-of-plane antiferroelectricity and the antiferroelectric–ferroelectric transition induced by the vertical external electric-field. The hidden out-of-plane antiferroelectricity and field induced ferroelectric polarization in spatial-inversion symmetric GeSe makes it a new member of van der Waals layered semiconductors with both in-plane and out-of-plane ferroelectricity, and possibly, can be extended to all group-IV monochalcogenides and other centrosymmetric van der Waals layered materials.

Van der Waals (vdW)-layered ferroelectric (FE) semiconductors, especially possessing the out-of-plane (OOP) FE property, hold great promise for fabricating next-generation nanodevices including compact non-volatile memory, nonlinear optical and optoelectronic devices, and in-memory computing with low-consumption. However, limited by the scarcity of candidates with broken spatial-inversion symmetry<sup>1</sup>, only a limited number of vdW OOP FE semiconductors have been confirmed<sup>2</sup>, such as  $\text{In}_2\text{Se}_3$ <sup>3,4</sup>,  $\text{CuInP}_2\text{S}_6$ <sup>5</sup> and  $\text{InSe}$ <sup>6</sup>, e.g., due to the ion displacement in the vertical direction<sup>3–5,7</sup> or the interlayer directional sliding (charge-redistribution)<sup>6,8–11</sup>, as well as those unique asymmetric artificial structures by interlayer twisting (with moiré patterns)<sup>12,13</sup>. As a newly-attractive vdW-layered family, anisotropic group-IV monochalcogenide MX (e.g., M = Ge, Sn; X = S, Se) semiconductors possess intriguing electric/optical properties, including in-plane AFE/FE and even multiferroicity<sup>14–16</sup>, since monolayer MX with a puckered structure along the armchair direction possesses in-plane spontaneous polarization and

FE property<sup>17–21</sup>. However, all reports involving AFE/FE in MX were in-plane, regardless of theoretical<sup>17,22,23</sup> and experimental<sup>20,21,24–27</sup> results in either monolayer or multilayer systems, except for the extrinsic OOP FE in SnSe that was induced by charge doping<sup>14</sup> and the mechanical force induced OOP FE in GeSe attributed to the Janus state<sup>28</sup>. In contrast, no intrinsic OOP FE can be accessible and even expectable in MX because of the facts that vdW-layered MX are interlayer inversion-symmetric and the vertical dipoles between anions and cations are antiparallely arranged both in intralayer and interlayer, which structurally gives a zero OOP electric polarization both in each-layer and vdW-interlayer, correspondingly resulting in a non-polar feature in the vertical direction.

Here, we uncover the unconventional intrinsic OOP AFE property in GeSe as an example of centrosymmetric vdW-layered semiconductors, a representative member of the MX family. AFE–FE transformation and simultaneous polarization reversal are theoretically predicted and experimentally realized on GeSe flakes with the

<sup>1</sup>Key Laboratory of Polar Materials and Devices (MOE), School of Physics and Electronic Science, East China Normal University, Shanghai 200241, China.

<sup>2</sup>Engineering Research Center of Nanophotonics & Advanced Instrument (MOE), School of Physics and Electronic Science, East China Normal University, Shanghai 200241, China. <sup>3</sup>These authors contributed equally: Fengrui Sui, Yilun Yu, Ju Chen. ✉e-mail: [rjq@ee.ecnu.edu.cn](mailto:rjq@ee.ecnu.edu.cn); [sjgong@ee.ecnu.edu.cn](mailto:sjgong@ee.ecnu.edu.cn); [fyyue@ee.ecnu.edu.cn](mailto:fyyue@ee.ecnu.edu.cn)

vertical external electric field, which can be attributed to the switchable structure distortion with asymmetric ion displacements of both cations (Ge) and anions (Se). Our investigation not only proposes a vdW-interlayer interaction induced unique origination of OOP AFE and the AFE-FE transition induced by external electric fields, but will also promote the follow-ups for practical application of them in low-consumption in-memory sensing and computing chips.

## Results

### Structure and optical characterizations

VdW-layered GeSe belongs to orthorhombic space group *Pnma* (Supplementary Fig. 1). The two principal axes along [010] and [100] named as the armchair and zigzag directions (Fig. 1a, d), respectively, can be confirmed by HAADF-STEM images (Fig. 1b, e) and the corresponding atomic-level energy dispersion spectroscopy (EDS) maps (Fig. 1c, f). Structurally, it exhibits an in-plane electric polarization along the armchair direction in each single layer with antiparallel arrangements between adjacent layers, showing interlayer AB-type stacking mode<sup>21,29,30</sup>, but no OOP electric polarization can be expected because the dipoles of anions and cations are antiparallely arranged in the vertical direction, both in each single layer (red arrows) and vdW-gap layer (purple arrows), by referring to the atomic models projecting along the zigzag direction (Fig. 1e, f). The lattice parameters determined are  $a = 0.438$  nm,  $b = 0.382$  nm, and  $c = 1.079$  nm with an almost equal spacing/thickness ( $\sim 2.4\%$  difference) between interlayer ( $-0.273$  nm) and intralayer ( $-0.266$  nm). This rather narrow vdW-gap may suggest a relatively strong interlayer vdW-force interaction accompanying with interlayer charge-redistribution, as predicted theoretically<sup>31</sup> that accounts for the difficulty to mechanically exfoliate GeSe into ultrathin- or mono-layer in experiments. X-ray diffraction (XRD) pattern demonstrates preferred reflections along (00*l*) planes

of the layered single-crystalline GeSe (Fig. 1g), indexing to the  $\alpha$ -GeSe (JCPDS No. 48-1226, *Pnma* 62), consistent with the results of HAADF-STEM.

We confirm the in-plane polarization vectors in anisotropic GeSe by angle ( $\theta$ )-resolved polarization Raman spectroscopy (Fig. 1h, Methods and Supplementary Fig. 2), where  $\theta = 0$  means the linearly polarized light parallels to the armchair direction (same in the following) and is verified by HAADF-STEM. Three strong Raman modes ( $A_g^1$  at  $\sim 81$   $\text{cm}^{-1}$ ,  $B_{3g}$  at  $\sim 150$   $\text{cm}^{-1}$  and  $A_g^3$  at  $\sim 189$   $\text{cm}^{-1}$ ) and a weak one ( $A_g^2$  at  $\sim 175$   $\text{cm}^{-1}$ ) with specified symmetry under different configurations characterize the optical anisotropy of GeSe, where  $A_g^3$  is the in-plane vibration along armchair direction<sup>23,32–34</sup> (Supplementary Fig. 2 and Supplementary Note 1) and  $B_{3g}$  predominant only in cross configuration points to the in-plane vibration along zigzag direction<sup>35</sup>. Based on this, polarization transmission spectra are obtained by fixing the polarization of incident photons parallel to either armchair or zigzag directions at different temperatures (Fig. 1i and Supplementary Fig. 3). We observe a giant energy difference of  $\sim 120$  meV between the two transmission edges corresponding to the optical bandgaps along armchair and zigzag directions, as shown by Tauc-plots (Fig. 1i, inset)<sup>36</sup>. This also reflects the strong in-plane optical anisotropy in orthorhombic GeSe. Notice that temperature-dependent Raman results disclose the ultrastability of  $\alpha$ -GeSe up to 700 K (Supplementary Fig. 4), and the in-plane optical anisotropy is repeatable in GeSe flakes with different thicknesses, similar to that in  $\text{ReSe}_2$ <sup>37</sup>.

### First-principles calculations

To explore the possible OOP AFE or FE in GeSe, we calculate the electrostatic potential energy distribution in a freestanding GeSe monolayer and a freestanding AB-stacking bilayer GeSe. For the

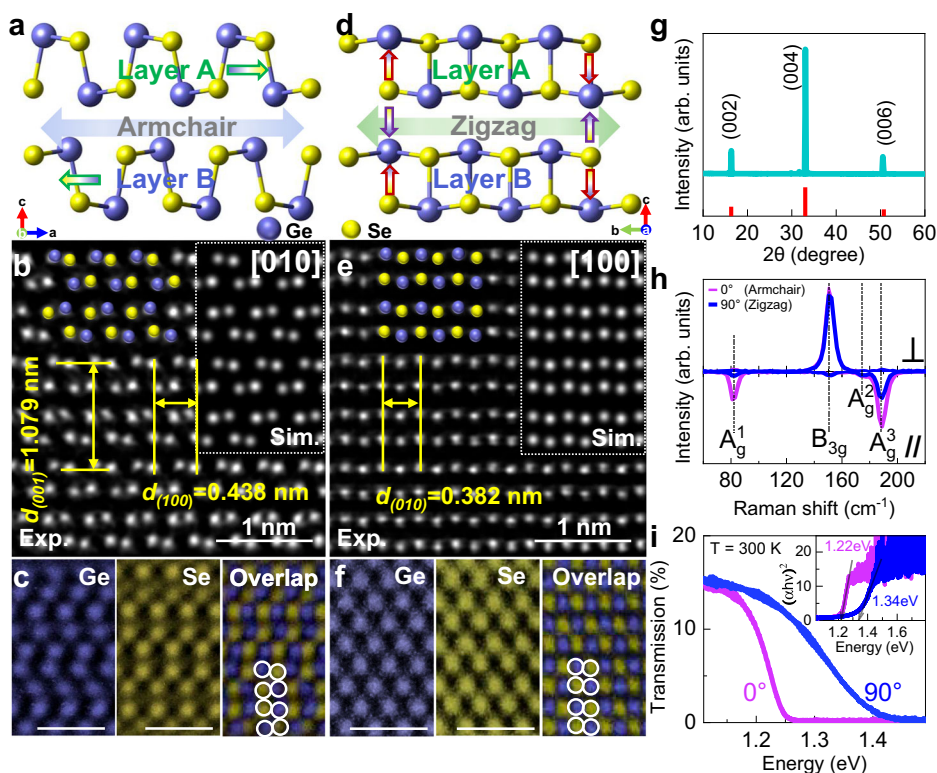


**Fig. 1 | Structural and optical characterizations of GeSe.** **a, d** The side-views of the atomic structures along armchair (**a**) and zigzag (**d**) directions. **b, e** HAADF-STEM images and corresponding atomic-level EDS maps (**c, f**) of GeSe along [010] (armchair direction, **b**) and [100] zone axis (zigzag direction, **e**) (where the armchair/zigzag direction is along the  $b/a$  lattice vector, respectively), where the insets

in **b, e** are the simulated HAADF-STEM images. The scale bars are 1 nm. **g** The XRD pattern from the (00*l*) surface. **h** Linearly polarized Raman spectra along armchair ( $\theta = 0$ ) and zigzag ( $\theta = 90$ ) directions in either parallel (//) or cross (⊥) geometries at 300 K. **i** Linearly polarized transmission spectra along armchair and zigzag directions at 300 K, together with Tauc-plot as the inset.

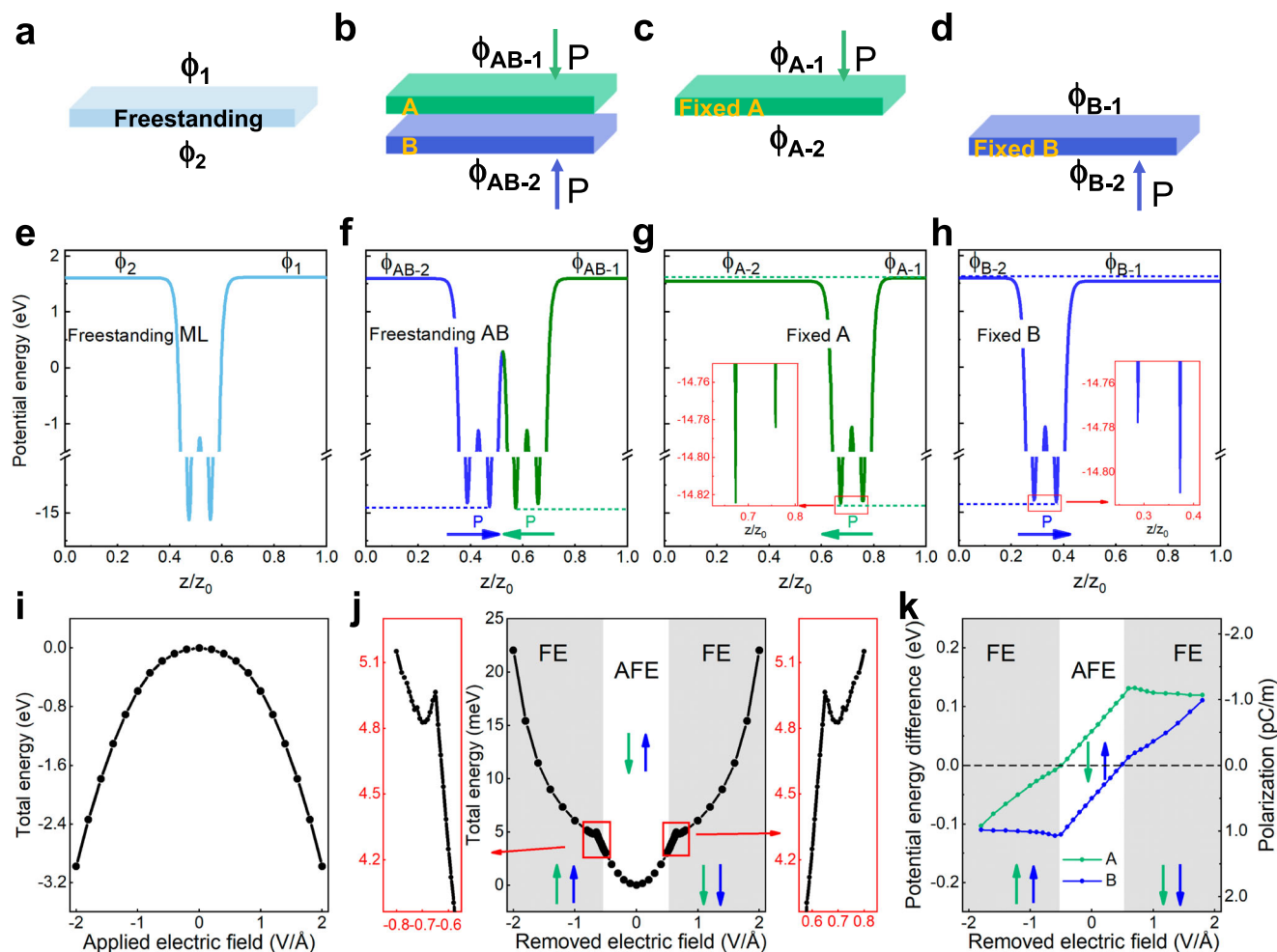


**Fig. 2 | Intrinsic OOP AFE in bilayer GeSe by first-principles calculations.**

**a** Freestanding monolayer (ML). **b** freestanding AB-stacking bilayer. **c** Fixed A layer in bilayer GeSe in **(b)**. **d** Fixed B layer in bilayer in **(b)**. The  $\phi_i$  ( $i = 1, 2, A-1, A-2, B-1, B-2, AB-1, AB-2$ ) in **a–d** indicates the vacuum energy level. **e–h** Electrostatic potential energy of the freestanding monolayer (**e**), AB-stacking bilayer (**f**), the fixed A layer (**g**), and the fixed B layer (**h**), where  $z_0$  is the thickness of the unit cell,  $z$  is a

coordinate variable, and  $z/z_0$  refers to the relative position in the unit cell. **i** Total energy of bilayer GeSe with external electric fields. **j** Total energy of bilayer GeSe with removal of the external electric fields yet preserving the electric field-tuned structures of the bilayer. The curves around the critical electric fields are highlighted by red squares and magnified panels. **k** Electric field dependence of the potential energy difference and the polarization for the A and B layers.

freestanding monolayer (Fig. 2a), the vacuum energy levels of its two surfaces are equal, i.e.,  $\phi_1 = \phi_2$  (Fig. 2e), indicating that there is no OOP polarization. Freestanding bilayer GeSe (Fig. 2b) with  $\phi_{AB-1} = \phi_{AB-2}$  also does not show net OOP polarization (Fig. 2f). However, the unequal potential wells of bilayer GeSe indicated by green and blue dotted lines imply that the net OOP polarization exists in the individual A and B layers, and the opposite polarization directions in A and B layers manifest the AFE feature (Fig. 2f). To confirm this AFE feature in bilayer GeSe, we remove B layer and fix A layer (Fig. 2c), or remove A layer and fix B layer (Fig. 2d). In the potential energy profiles of the fixed A (Fig. 2g) and B layer (Fig. 2h), we can see that  $\phi_{A-1} > \phi_{A-2}$  and  $\phi_{B-1} < \phi_{B-2}$ , which means that there is net polarization in A(B) layer pointing from  $A_1$  ( $B_2$ ) to  $A_2$  ( $B_1$ ) surface.

We then explore the OOP polarization evolution in bilayer GeSe in response to the vertical external electric field ( $E_{OOP}$ ) (Fig. 2i–k). Within the whole work, the direction pointing from B to A is defined as the positive electric field. The external electric field will redistribute the electrostatic potential and slightly change the atomic positions. For each electric field, we can obtain a new structure for bilayer GeSe according to the structure relaxation (Methods). The relation between the total energy of bilayer GeSe and external electric fields can be well described by a parabolic curve (Fig. 2i). We then remove the external electric fields, fix each bilayer structure tuned by

the external electric field, and calculate the total energy (Fig. 2j). Through this approach, we can confirm the AFE state corresponding to the lowest energy and find the two metastable FE states, which are induced by the external electric field, yet can be preserved when the external electric field is removed (Fig. 2j together with amplified panels at both sides). We also explore dependence of the potential energy difference  $\Delta\phi$  on the external electric fields for the individual A and B layers, with  $\Delta\phi(A) = \phi_{A-1} - \phi_{A-2}$  and  $\Delta\phi(B) = \phi_{B-1} - \phi_{B-2}$  (Fig. 2k). In 2D materials, the OOP polarization ( $P_z$ ) can be easily evaluated by the simple equation,  $P_z = \epsilon_0 \Delta\phi$ , where  $\epsilon_0$  is the vacuum dielectric constant and  $\Delta\phi$  is the potential energy difference<sup>38</sup>. When the external electric field  $E_{OOP} = 0$ ,  $\Delta\phi(A) = -\Delta\phi(B) = 0.057$  eV, indicating the opposite OOP polarization in A and B layers with  $P_z = \pm 0.505$  pC/m. It is desirable that an external electric field can reverse the OOP polarization in one layer, inducing the AFE/FE transition. According to the calculations, we find that the left critical point corresponds to  $E_{OOP} = -0.65$  V/Å and  $\Delta\phi(A) = 0$  (the right critical point corresponds to  $E_{OOP} = 0.65$  V/Å and  $\Delta\phi(B) = 0$ ). When the external electric field is larger than the critical value, the OOP polarizations in the A and B layers turn from antiparallel to parallel, i.e., AFE becomes FE. The saturated value of  $\Delta\phi(A)$  and  $\Delta\phi(B)$  is about 0.12 eV, corresponding to 1.06 pC/m in the individual A and B layer, and 2.12 pC/m in bilayer GeSe.



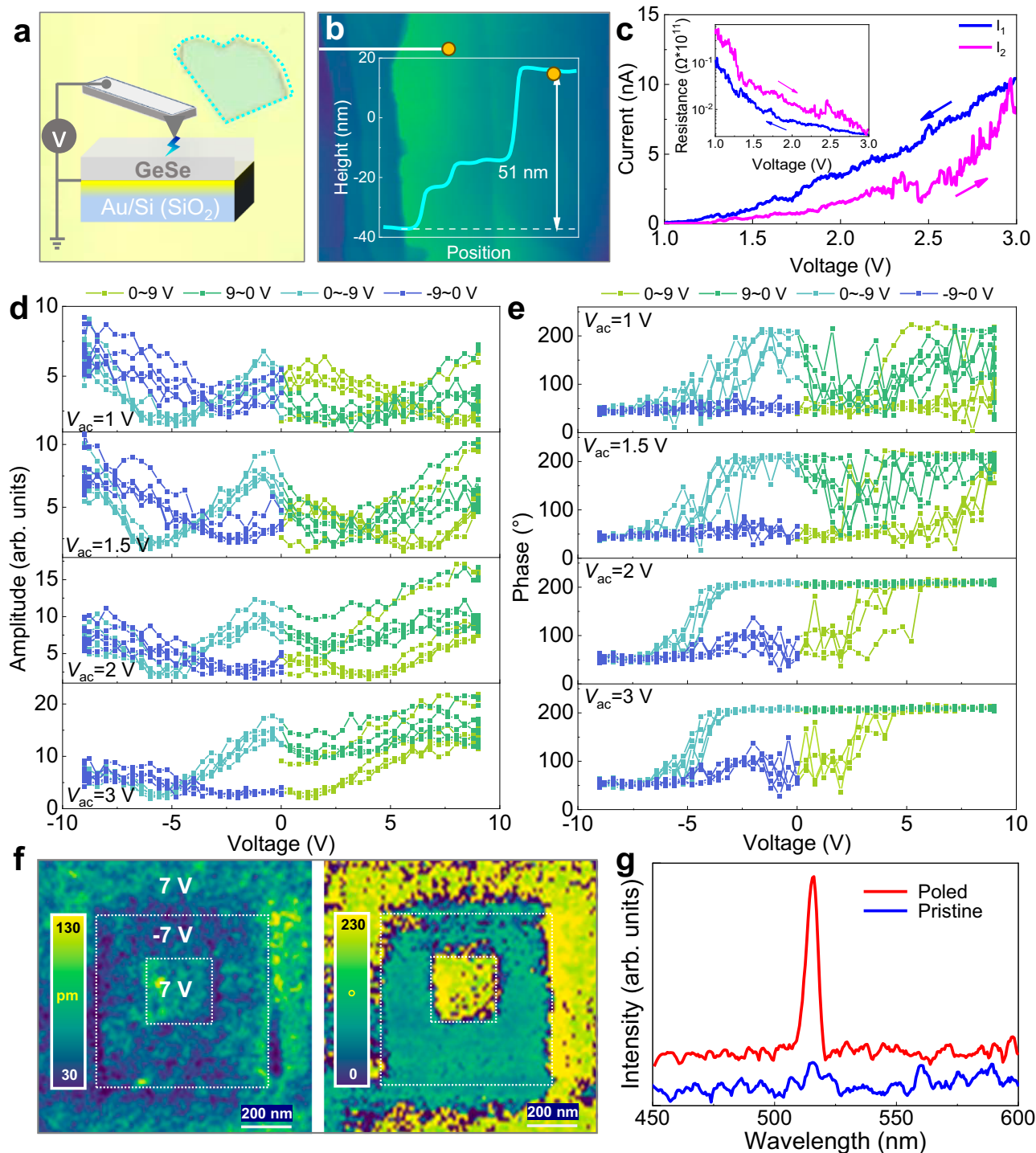


**Fig. 3 | Intrinsic OOP AFE and AFE-FE transition in GeSe.** **a** Schemes of the setup for PFM/CAFM measurements of GeSe flake together with the OM image. **b** AFM image of GeSe flake with a thickness of 51 nm. **c** The I-V loop from CAFM measurements. Inset for the corresponding R-V curve derived from the I-V loop. The pink arrows show the current jumps as the voltage increases (pink curve), corresponding to the abrupt resistance changes in the R-V curve. **d, e** A series of local PFM amplitude (**d**) and phase (**e**) loops during the switching process of the GeSe

flake in **a** at different  $V_{ac}$ . **f** The FE polarization switching for GeSe flake by using PFM domain writing technique. Domains are written on GeSe flake with reverse dc biases of -7 and 7 V. The PFM amplitude (left) and phase (right) maps show the corresponding poled areas, in which a clear domain wall can be seen in the phase map. **g** SHG spectra. Blue/red curves for pristine/poled GeSe flakes, respectively, with the same experimental conditions.

### PFM results

Next, we perform PFM and conductive atomic force microscopy (CAFM) measurements (Fig. 3a and Methods) to explore the OOP AFE/FE property in GeSe. The I-V curves by CAFM with voltages sweeping on a 51-nm-thick GeSe flake (Fig. 3b) demonstrate distinctive hysteresis features, as representatively shown in Fig. 3c together with the

corresponding resistance changes during forward/reverse voltage sweeping (as inset), exhibiting the FE behavior. Additional CAFM curves can also be detected on GeSe flakes with different thicknesses (Supplementary Fig. 5). Intriguingly, the corresponding PFM results for the same flake in Fig. 3b demonstrate a rather complicated vertical voltage-dependent hysteresis loop with the direct voltage ( $V_{dc}$ ) cyclically

sweeping from  $-9$  V to  $+9$  V and varying  $ac$  voltages ( $V_{ac} = 1-3$  V) under the tip-sample contact resonant frequency ( $\sim 240$  kHz) (Fig. 3d, e). The AFE-like double hysteresis loops with four characteristic amplitude peaks can be clearly observed at low alternating voltages (e.g.,  $V_{ac} = 1$  V; Fig. 3d, top panels). However, at high alternating voltages, the double butterfly-type amplitude loops evolve into the single butterfly-type amplitude loops that typically manifest the conventional FE behavior (e.g.,  $V_{ac} = 3$  V; Fig. 3d, bottom panels). Simultaneously, the phase loops switch  $180^\circ$  almost twice at first but then only one time during cyclically sweeping  $V_{dc}$  (Fig. 3e). These behaviors, including the voltage-dependent amplitude and phase evolutions, evidently suggest the OOP AFE-FE transition, providing solid experimental evidences on intrinsic OOP AFE and field-induced AFE-FE transition in vdW GeSe, as exactly predicted by our foregoing first-principles calculations. Additional PFM measurements (Supplementary Figs. 6, 7) and domain writing results (Fig. 3f) further confirm the electric field induced OOP FE in GeSe is room temperature robust with good retention. The second harmonic generation (SHG; Fig. 3g and Supplementary Note 3) spectra obtained on GeSe flake before and after poling indicate the vertical external electric field induced spatial symmetry breaking.

### Mechanism analysis

Based on the above first-principles calculations, we conclude that the AFE-FE transition of GeSe under the external electric field is strongly related to the microstructural distortion induced by the external electric field. We perform comprehensive HAADF-STEM analyses to directly observe the atomic configuration evolution (Methods and Supplementary Note 4). We first perform atomic-level in situ biasing STEM analyses to catch the dynamic microstructure changes in GeSe in response to the external electric field. As shown in Supplementary Fig. 8, atomic-level HAADF images obtained at the  $I-t$  mode clearly show distorted atomic arrangement evolutions in GeSe. To get higher quality and stable atomic images, quasi in situ HAADF analyses are further executed. Taking advantage of the polarization (structure) nonvolatility feature of FE materials, we first pole different areas on the GeSe flake with opposite biases on the PFM system and then prepare TEM samples at the specific poled areas by using focused ion beam (FIB) technique (Supplementary Fig. 9), so that the corresponding atomic configuration with different polarization states can be traced. As shown in Fig. 4a–c, we find the bias can shift Ge and Se atoms, and the opposite bias induces reverse changes. This can result in a distorted atomic arrangement in GeSe, pointing to two vertical opposite FE states (Fig. 4a, c). To clearly view the atomic displacements (atomic positions and changes in Ge-Se bonding angles in each single layer) and the accompanying polarization evolution driven by the external electric field, we perform detailed atomic arrangement analyses for HAADF-STEM images (Fig. 4d–f) combining with atomic quantification via Calatom software based on custom MATLAB scripts (Supplementary Figs. 10, 11 and Supplementary Note 4)<sup>39</sup>. We then schematically draw the four Ge-Se bonding models (Supplementary Fig. 12a) and mark the polarization using white arrows over the HAADF images taken at the pristine and poled states. At the pristine state, adjacent GeSe layers present the same in-plane and OOP polarization intensity while with different directions, demonstrating in-plane and OOP AFE features. When a bias is applied, Ge-Se bonding of I and III becomes steeper, while Ge-Se bonding of II and IV gets flatter (Fig. 4a, inset), leading to obvious Ge-Se-Ge-Se bonding angles change (left panels in Fig. 4d–f and Supplementary Fig. 12). This enhances the OOP polarization of each single layer, and finally adjacent layers will present same polarization directions, resulting in FE states. The opposite phenomenon is obtained when a reverse bias is applied (Fig. 4c, inset). The FE states present alternating vdW-gaps (Supplementary Fig. 13).

The calculated atomic structures under different external electric fields (Fig. 4g–i and Supplementary Fig. 14) show similar microstructural changes. Without the external electric field (Fig. 4h), in layer

A (B), the center charge of Ge is below (above) that of Se, indicating opposite polarizations in A and B layers. Under the external electric fields, the steeper I/III Ge-Se bonding in Fig. 4g (or steeper II/IV Ge-Se bonding in Fig. 4i) results in the center charge of Ge above (or below) that of Se, which indicates that the polarization is upward (or downward) in both A and B layers, presenting distinct FE states. In addition, we find the electric fields enhance the charge center difference to be around  $\pm 0.028$  Å, which is only about  $\pm 0.014$  Å at the pristine state, indicating that the external electric field not only reverses the polarization direction but also enhances its magnitude. Atomic structures in Fig. 4g, i agree well with the observation of STEM images in Fig. 4a, c, and the polarization evolution derived from the microstructures is consistent with that from the potential energy analysis (Fig. 2k).

### Discussion

In summary, we theoretically predict the OOP AFE in orthorhombic vdW GeSe semiconductor, which structurally possesses a zero OOP electric dipole both in intralayer and interlayer, and experimentally confirm the hidden OOP AFE and its evolution into FE states subjected to the external electric field. The origination of this unconventional OOP AFE is due to the interlayer vdW interaction induced different potential distributions between the upper and lower surfaces of each layer, leading to a net OOP electric polarization of single-layer but with opposite polarization vectors between adjacent layers, i.e., the intrinsic OOP AFE. A vertical electric field can result in asymmetric ion displacements, including both cations and anions along the electric field direction, pointing to two opposite polarization states. The atomic-level microstructure changes in the in situ biasing STEM system directly reveal the fine microstructure distortions during the AFE-FE transition, of which the unimaginable asymmetric displacements of the anions and cations due to the vertical electric field are rather consistent with the prediction of our first-principles calculations. These self-consistent results from experiment and theory not only confirm the intriguing intrinsic OOP AFE in GeSe and the potential application in in-memory computing based on MX compounds like GeSe, but also provide a novel strategy toward polarization modulation in structurally symmetric vdW-layered materials<sup>40</sup>.

### Online content

Any methods, additional references, Nature Research reporting summaries, source data, extended data, supplementary information, acknowledgements, peer review information; details of author contributions and competing interests; and statements of data and code availability are available at xxx.

### Methods

#### Sample preparation and transfer

For optical (including Raman, transmission, and SHG) and electric (PFM) characterizations, GeSe flakes with different thicknesses are prepared from bulk GeSe single crystal via mechanical exfoliation.

#### FE characterizations

PFM measurements procedures were reported in our previous work<sup>6</sup> using an adjusted  $ac$  voltage ( $V_{ac} = 1-3$  V) to detect the evolution of AFE-FE in GeSe, and using reverse  $dc$  biases ( $V_{dc} = \pm 7$  V) for domain writing. The conductive tips (AC240TM, Olympus) are utilized during the measurements. The tip cantilever length and width are 240 and 40  $\mu\text{m}$ , respectively. The tip radius and height are 28 nm and 14  $\mu\text{m}$ , respectively.

The room temperature  $I-V$  curves are recorded in a CAFM mode. Bias sweeps are applied to the sample from the internal source, and the current is measured through commercial conductive Pt-coated silicon cantilevers by the internal lock-in units of the AFM. The bias sweeps are set as a positive to negative voltage circle, like 0 to  $+1.5$  V

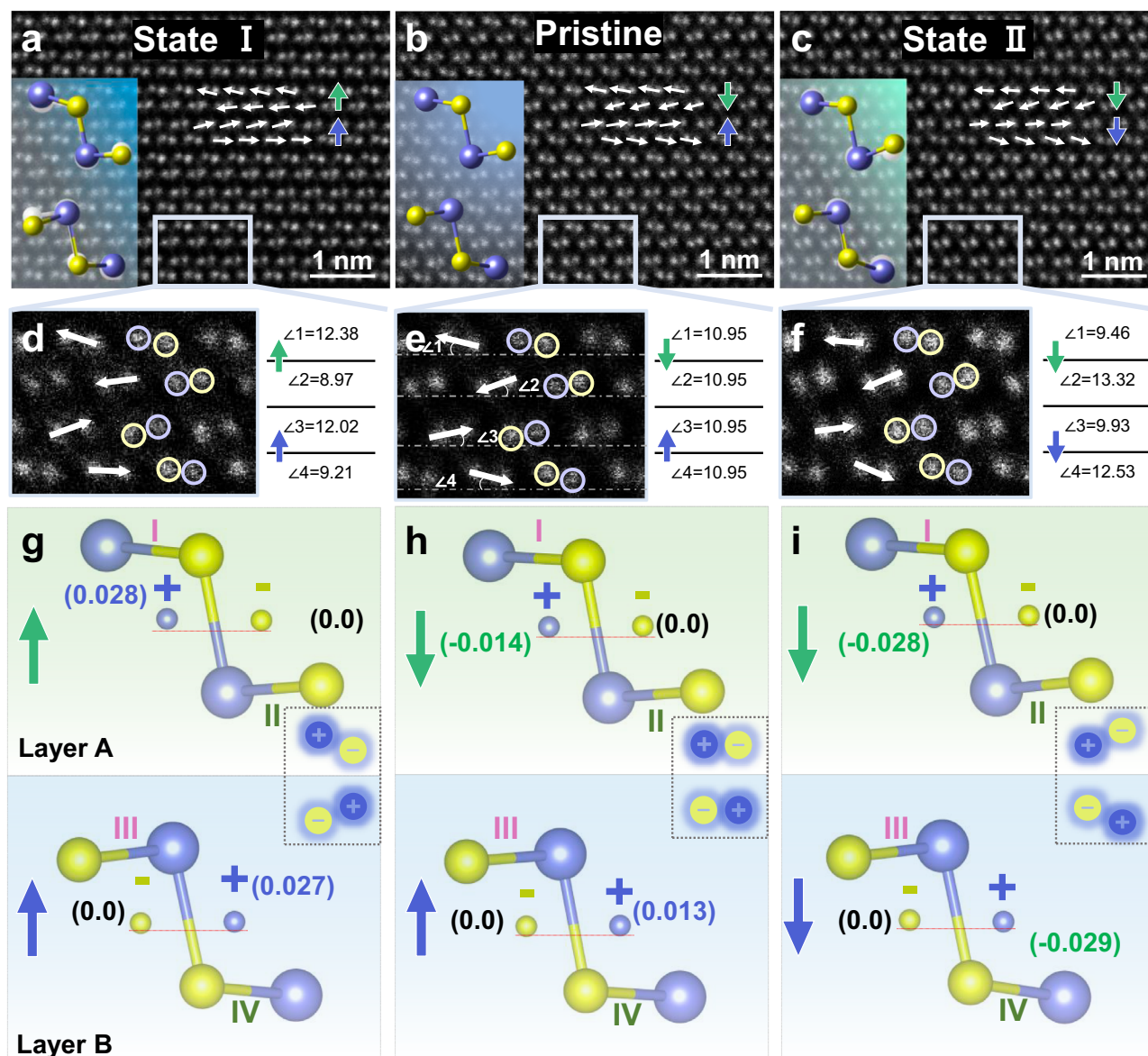


**Fig. 4 | Microstructural changes of GeSe at different FE states.** **a–c** HAADF images of GeSe flake at different FE states (**a** for State I, **b** for pristine, **c** for State II). Insets are schematic atomic models of GeSe at different poled states. **d–f** Zoom-in HAADF images of areas marked as rectangles in (**a–c**). The dotted white lines are used to display the angles 1–4. The Ge–Se–Ge–Se bonding angle changes are displayed in the left panels of the corresponding HAADF images. **g–i** Calculated

atomic structures of bilayer GeSe under different external electric-fields. The dotted horizontal dashed line in each sub-panel is used to recognize the relative position of the charge center along the *z* direction (accurately marked by the absolute values). Insets show the charge center structures. The bonds in **a–f** are marked by tilted white arrows, and the net polarization of the adjacent layers in **a–i** are indicated by green and blue bold arrows.

to  $-1.5$  to  $0$  V, with a time period of  $1$  s, and the currents are measured with a limit of  $10.4$  nA.

Poling areas for SHG analyses and TEM sample preparation are performed with the PFM tip carries reverse *dc* biases ( $V_{dc}$ ). The normal contact force is around  $40$  nN.

### Structural and chemical composition analyses

XRD patterns are obtained on the Bruker D8 Discover (Germany).

TEM lamellae are prepared by the FIB technique on a Helios G4 UX (FEI, USA). HAADF imaging is performed on a spherical aberration TEM (JEOL Grand ARM300, Japan) with a JEOL dual  $158$  mm<sup>2</sup> SDD detector for atomic-level EDS mapping.

In situ biasing observations are performed using a PicoFemto holder from ZepTools Technology Company. The STEM image simulation and analyses processes were reported in our previous work<sup>6</sup>.

### Optical characterizations

Raman spectra are obtained by a  $\mu$ -Raman system with a back-scattering configuration (Renishaw inVia Reflex, UK) using a  $532$  nm linearly polarized laser as the excitation source. To avoid possible damage to the samples, the laser power is set below  $1$  mW. Both excitation and scattered optical paths are equipped with polarizers. Controlling both polarizers can provide specified configurations: parallel ( $//$ ) and cross ( $\perp$ ). The sample holder is rotatable in the plane perpendicular to the incident laser.

Angle-resolved polarization optical transmission spectra are recorded on a Fourier transform infrared (FTIR) spectrometer (Bruker Vertex 80 v, Germany), which covers the wavelength range of  $\sim 0.4$ – $15$   $\mu$ m by combining with different light sources, beam splitters, and detectors. The incident light path is equipped with a linear polarizer (Thorlabs LPNIR100-MP2, USA) with a wavelength response range from  $750$  to  $1800$  nm. The sample holder can be rotated to



control the angle between the sample crystal axis and the polarization direction of the incident light.

SHG measurements are performed on the pristine and poled (domain written) areas with a confocal microscope setup in reflection geometry. A 1030 nm pulsed laser (pulse width 100 fs, repetition frequency 80 MHz) is used as the excitation source.

### DFT calculations

The calculations are performed within density-functional theory (DFT) by the projector-augmented wave (PAW) method implemented in the Vienna ab initio simulation package (VASP), and the generalized gradient approximation (GGA) is used. The energy cutoff of 500 eV is used for the plane-wave basis expansion with the total energy convergence criterion of  $10^{-5}$  eV per unit cell. A  $\Gamma$ -centered  $k$ -grid  $20 \times 20 \times 1$  is used to sample the 2D Brillouin zone. For geometry optimization, all the internal coordinates are relaxed until the Hellmann–Feynman forces are less than 1 meV/Å. The dispersion-corrected DFT-D2 method is introduced in first-principles calculations to relax the structure of the bilayer system. A large enough vacuum thickness (20 Å) along the  $z$ -axis is adopted to avoid the interaction between adjacent unit cells.

### Reporting summary

Further information on research design is available in the Nature Portfolio Reporting Summary linked to this article.

### Data availability

All data were available in the main text or the Supplementary Material.

### References

- Zhang, D., Schoenherr, P., Sharma, P. & Seidel, J. Ferroelectric order in van der Waals layered materials. *Nat. Rev. Mater.* **8**, 25–40 (2022).
- Wang, C., You, L., Cobden, D. & Wang, J. Towards two-dimensional van der Waals ferroelectrics. *Nat. Mater.* **22**, 542–552 (2023).
- Cui, C. et al. Interrelated in-plane and out-of-plane ferroelectricity in ultrathin two-dimensional layered semiconductor  $\text{In}_2\text{Se}_3$ . *Nano Lett.* **18**, 1253–1258 (2018).
- Ding, W. et al. Prediction of intrinsic two-dimensional ferroelectrics in  $\text{In}_2\text{Se}_3$  and other  $\text{III}_2\text{VI}_3$  van der Waals materials. *Nat. Commun.* **8**, 14956 (2017).
- Liu, F. et al. Room-temperature ferroelectricity in  $\text{CuInP}_2\text{S}_6$  ultrathin flakes. *Nat. Commun.* **7**, 12357 (2016).
- Sui, F. et al. Atomic-level polarization reversal in sliding ferroelectric semiconductors. *Nat. Commun.* **15**, 3799 (2024).
- Han, W. et al. Phase-controllable large-area two-dimensional  $\text{In}_2\text{Se}_3$  and ferroelectric heterophase junction. *Nat. Nanotechnol.* **18**, 55–63 (2023).
- Vizner Stern, M. et al. Interfacial ferroelectricity by van der Waals sliding. *Science* **372**, 1462–1466 (2021).
- Meng, P. et al. Sliding induced multiple polarization states in two-dimensional ferroelectrics. *Nat. Commun.* **13**, 7696 (2022).
- Rogee, L. et al. Ferroelectricity in untwisted heterobilayers of transition metal dichalcogenides. *Science* **376**, 973–978 (2022).
- Deb, S. et al. Cumulative polarization in conductive interfacial ferroelectrics. *Nature* **612**, 465–469 (2022).
- Yasuda, K., Wang, X., Watanabe, K., Taniguchi, T. & Jarillo-Herrero, P. Stacking-engineered ferroelectricity in bilayer boron nitride. *Science* **372**, 1458–1462 (2021).
- Zheng, Z. et al. Unconventional ferroelectricity in moiré heterostructures. *Nature* **588**, 71–76 (2020).
- Du, R. et al. Two-dimensional multiferroic material of metallic  $p$ -doped  $\text{SnSe}$ . *Nat. Commun.* **13**, 6130 (2022).
- Fei, R., Kang, W. & Yang, L. Ferroelectricity and phase transitions in monolayer group-IV monochalcogenides. *Phys. Rev. Lett.* **117**, 097601 (2016).
- Wu, M. H. & Zeng, X. C. Intrinsic ferroelasticity and/or multiferroicity in two-dimensional phosphorene and phosphorene analogues. *Nano Lett.* **16**, 3236–3241 (2016).
- Ronneberger, I., Zanolli, Z., Wuttig, M. & Mazzarello, R. Changes of structure and bonding with thickness in chalcogenide thin films. *Adv. Mater.* **32**, 2001033 (2020).
- Zhao, Y. F. et al. Raman spectra of bulk and few-layer  $\text{GeSe}$  from first-principles calculations. *Front. Mater.* **8**, 736057 (2021).
- Xu, B., Deng, J., Ding, X., Sun, J. & Liu, J. Z. Van der Waals force-induced intralayer ferroelectric-to-antiferroelectric transition via interlayer sliding in bilayer group-IV monochalcogenides. *npj Comput. Mater.* **8**, 47 (2022).
- Guan, Z. et al. Electric-field-induced room-temperature antiferroelectric-ferroelectric phase transition in van der Waals layered  $\text{GeSe}$ . *ACS Nano* **16**, 1308–1317 (2022).
- Luo, Y. et al. Electrically switchable anisotropic polariton propagation in a ferroelectric van der Waals semiconductor. *Nat. Nanotechnol.* **18**, 350–356 (2023).
- Mao, N. N. et al. Giant nonlinear optical response via coherent stacking of in-plane ferroelectric layers. *Adv. Mater.* **35**, 2210894 (2023).
- Chang, K. et al. Microscopic manipulation of ferroelectric domains in  $\text{SnSe}$  monolayers at room temperature. *Nano Lett.* **20**, 6590–6597 (2020).
- Shi, C. et al. Domain-dependent strain and stacking in two-dimensional van der Waals ferroelectrics. *Nat. Commun.* **14**, 7168 (2023).
- Higashitarumizu, N. et al. Purely in-plane ferroelectricity in monolayer  $\text{SnS}$  at room temperature. *Nat. Commun.* **11**, 2428 (2020).
- Guan, Z. et al. 2D Janus polarization functioned by mechanical force. *Adv. Mater.* **36**, 2403929 (2024).
- Cheng, M., Si, Y., Li, N. & Guan, J. Synergy of charged domain walls in 2D in-plane polarized ferroelectric  $\text{GeS}$  for photocatalytic water splitting. *J. Am. Chem. Soc.* **146**, 26567–26573 (2024).
- Chen, Y. et al. Ferroelectric-tuned van der Waals heterojunction with band alignment evolution. *Nat. Commun.* **12**, 4030 (2021).
- Sutter, P., Komsa, H. P., Lu, H., Gruverman, A. & Sutter, E. Few-layer tin sulfide ( $\text{SnS}$ ): Controlled synthesis, thickness dependent vibrational properties, and ferroelectricity. *Nano Today* **37**, 101082 (2021).
- Wang, J. J. et al. Strain-engineering on  $\text{GeSe}$ : Raman spectroscopy study. *Phys. Chem. Chem. Phys.* **23**, 26997–27004 (2021).
- Tang, K. W., Qi, W. H., Wei, Y. R., Ru, G. L. & Liu, W. M. High-throughput calculation of interlayer van der Waals forces validated with experimental measurements. *Research* **2022**, 9765121 (2022).
- Ribeiro, H. B., Ramos, S. L. L. M., Seixas, L., de Matos, C. J. S. & Pimenta, M. A. Edge phonons in layered orthorhombic  $\text{GeS}$  and  $\text{GeSe}$  monochalcogenides. *Phys. Rev. B* **100**, 094301 (2019).
- Zhou, Z. et al. Low symmetric sub-wavelength array enhanced lensless polarization-sensitivity photodetector of germanium selenium. *Sci. Bull.* **68**, 173–179 (2023).
- Hu, X. Z. et al. Salt-assisted growth of ultrathin  $\text{GeSe}$  rectangular flakes for phototransistors with ultrahigh responsivity. *ACS Appl. Mater. Interfaces* **11**, 23353–23360 (2019).
- Zhou, X. et al. Highly anisotropic  $\text{GeSe}$  nanosheets for phototransistors with ultrahigh photoresponsivity. *Adv. Sci.* **5**, 1800478 (2018).

36. Tauc, J., Grigorovici, R. & Vancu, A. Optical properties and electronic structure of amorphous germanium. *Phys. status solidi b* **15**, 627–637 (1966).
37. Yang, S. et al. Chiral phonon, valley polarization, and inter/intra-valley scattering in a van der Waals ReSe<sub>2</sub> semiconductor. *ACS Nano* **18**, 33754–33764 (2024).
38. Wang, Z. & Liu, Z. Novel piezoelectricity in two-dimensional metallic/semimetallic materials with out-of-plane polarization. *J. Phys. Chem. Lett.* **14**, 7549–7555 (2023).
39. Zhang, Q., Zhang, L. Y., Jin, C. H., Wang, Y. M. & Lin, F. CalAtom: A software for quantitatively analysing atomic columns in a transmission electron microscope image. *Ultramicroscopy* **202**, 114–120 (2019).
40. Ji, J., Yu, G., Xu, C. & Xiang, H. Fractional quantum ferroelectricity. *Nat. Commun.* **15**, 135 (2024).

## Acknowledgements

This work was financially supported by the National Natural Science Foundation of China grants 6227406, 62274066, and 12134003, the National Key Research Project of China grant 2022YFA1402902, the National Science Foundation of Chongqing, China grants CCSTB2023NSCQ-MSX0975, the East China Normal University Multifunctional Platform for Innovation (004), the Foundational Research Funds for the Central Universities grant YBNLTS2024-022, and the Open Fund of State Key Laboratory of Infrared Physics (Grant No. SITP-NLIST-ZD-2024-06). The authors are grateful for profitable discussions with Professors A. M. Rappe and X. G. Wan.

## Author contributions

F.Y. and R.Q. formulated and supervised the project. F.S., Y.Y., R.G., R.J., and B.L. prepared the samples. F.S., R.Q., B.L., R.G., and Y.Z. conducted the TEM investigations and characterizations. J.C. and S.G. performed the DFT calculations. R.Q., S.G., and F.Y. analyzed the data. R.Q., S.G., and F.Y. drafted the original manuscript. J.H.C. reviewed and edited the manuscript with contributions from all authors.

## Competing interests

The authors declare no competing interests.

## Additional information

**Supplementary information** The online version contains supplementary material available at <https://doi.org/10.1038/s41467-025-57138-5>.

**Correspondence** and requests for materials should be addressed to Ruijuan Qi, Shijing Gong or Fangyu Yue.

**Peer review information** *Nature Communications* thanks the anonymous, reviewer(s) for their contribution to the peer review of this work. A peer review file is available.

**Reprints and permissions information** is available at <http://www.nature.com/reprints>

**Publisher's note** Springer Nature remains neutral with regard to jurisdictional claims in published maps and institutional affiliations.

**Open Access** This article is licensed under a Creative Commons Attribution-NonCommercial-NoDerivatives 4.0 International License, which permits any non-commercial use, sharing, distribution and reproduction in any medium or format, as long as you give appropriate credit to the original author(s) and the source, provide a link to the Creative Commons licence, and indicate if you modified the licensed material. You do not have permission under this licence to share adapted material derived from this article or parts of it. The images or other third party material in this article are included in the article's Creative Commons licence, unless indicated otherwise in a credit line to the material. If material is not included in the article's Creative Commons licence and your intended use is not permitted by statutory regulation or exceeds the permitted use, you will need to obtain permission directly from the copyright holder. To view a copy of this licence, visit <http://creativecommons.org/licenses/by-nc-nd/4.0/>.

© The Author(s) 2025, corrected publication 2025